JACS
JOURNAL OF THE AMERICAN CHEMICAL SOCIETY
pubs.acs.org/JACS
Article

Attenuating Imine Bond Polarization in Covalent Organic Frameworks Accelerates Charge and Proton Transport for High-Efficiency Photocatalytic Hydrogen Evolution

Zhipeng Luo,[○] Chao Li,[○] Wanxiang Yang,[○] Yu Chang,[○] Kai-Ling Wu, Liwei Xia, Jingru Gao, Fengtao Zhang, Qiwei Duan, Sibo Wang, Zailai Xie, Xiaofeng Wu, Guan-E Wang, Wei Lin,* Teng-Teng Chen,* Mingfei Zhou, Yihan Zhu,* Gang Xu, and Xiong Chen*

Cite This: https://doi.org/10.1021/jacs.6c04124
Read Online

ABSTRACT: While the structural tunability and π-electron delocalization of covalent organic frameworks (COFs) make them promising candidates for photocatalytic hydrogen evolution, the intrinsic polarization of their imine bonds often impedes efficient charge separation and transport. To overcome this fundamental kinetic barrier, we report a molecular engineering strategy that attenuates imine bond polarization through the functionalization of COF pore walls with electron-donating methoxy (−OMe) motifs. This structural modulation significantly enhances π-conjugation and interlayer interactions, promoting efficient charge separation and extending charge carrier lifetimes. Furthermore, the methoxy groups facilitate optimal proton transport by establishing an ordered hydrogen-bond network. Ultrafast transient absorption spectroscopy and proton conductivity measurements conclusively verify the generation of long-lived polarons and rapid proton hopping within the framework. Consequently, the engineered methoxy-functionalized COF achieves an exceptional photocatalytic hydrogen evolution rate of ca. 100 mmol h^{-1} g_{cat}^{-1} and an apparent quantum yield of 21.8 ± 0.80% at 450 nm, vastly outperforming its neutral and electron-withdrawing counterparts. These mechanistic insights provide a dependable blueprint for the rational design of high-performance imine-linked COF photocatalysts.

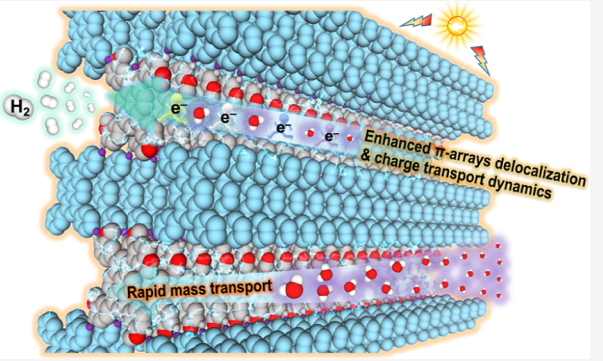

INTRODUCTION

The increasing scarcity of primary energy resources and escalating environmental pollution pose critical barriers to sustainable development, driving an urgent need for clean, renewable energy technologies. Photocatalysis offers a compelling solution by directly converting abundant solar energy into storable chemical fuels, such as hydrogen.[1] Recently, covalent organic frameworks (COFs) have emerged as a highly attractive class of photocatalysts, distinguished by their well-defined structural motifs, permanent porosity, high crystallinity, and extensive π-electron delocalization.[2] However, despite rapid progress in COF-based water splitting,[3] their overall photocatalytic performance is frequently bottlenecked by intrinsic material limitations, particularly low dielectric constants and the rapid recombination of photogenerated charge carriers.[4] Addressing these constraints requires satisfying a complex set of kinetic and thermodynamic parameters, including suitable bandgap alignment, efficient light absorption, favorable hydrophilicity, and optimized charge and mass transport within the COF channels.[5]

Among the diverse library of COFs, imine-linked structures are some of the most extensively investigated photocatalysts.[3a,6] The reversible polycondensation of imine bonds yields the high crystallinity necessary for robust photocatalytic activity.[7,8] Additionally, the inherent polarization of the imine (C═N) bond—driven by the electronegativity difference between carbon and nitrogen—creates localized negative charges at the nitrogen sites, which thermodynamically favors proton attraction to trigger the hydrogen evolution half-reaction.[9] Paradoxically, this same polarization induces strong electrostatic repulsion between adjacent layers. This repulsion hinders optimal interlayer stacking and restricts intralayer π-delocalization, ultimately leading to sluggish charge mobility

Received: February 24, 2026
Revised: May 7, 2026
Accepted: May 11, 2026

Chart 1. (a) Synthetic Routes of Py-R−COFs (Atoms: Carbon in Py-NO_2, Py-H and Py-OMe (Gray); Carbon in PyTA (Light Cyan); Oxygen in Py-NO_2 and Py-OMe (Red); Nitrogen in Py-NO_2 and PyTA (Purple); Hydrogen (White)); (b) Resonance Effect of Oxygen Lone Pair Electrons Softens the Polarization Effect, the Typical Polarization Influence, Electron-Deficient Effect of Nitro Groups Aggravates the Polarization Influence of Imine-Linkage; (c) Photoinduced Charge Separation and Transfer for the Intralayer; (d) Rapid Mass Transport and Boosted π-Arrays Delocalization in the 1D Nanochannel

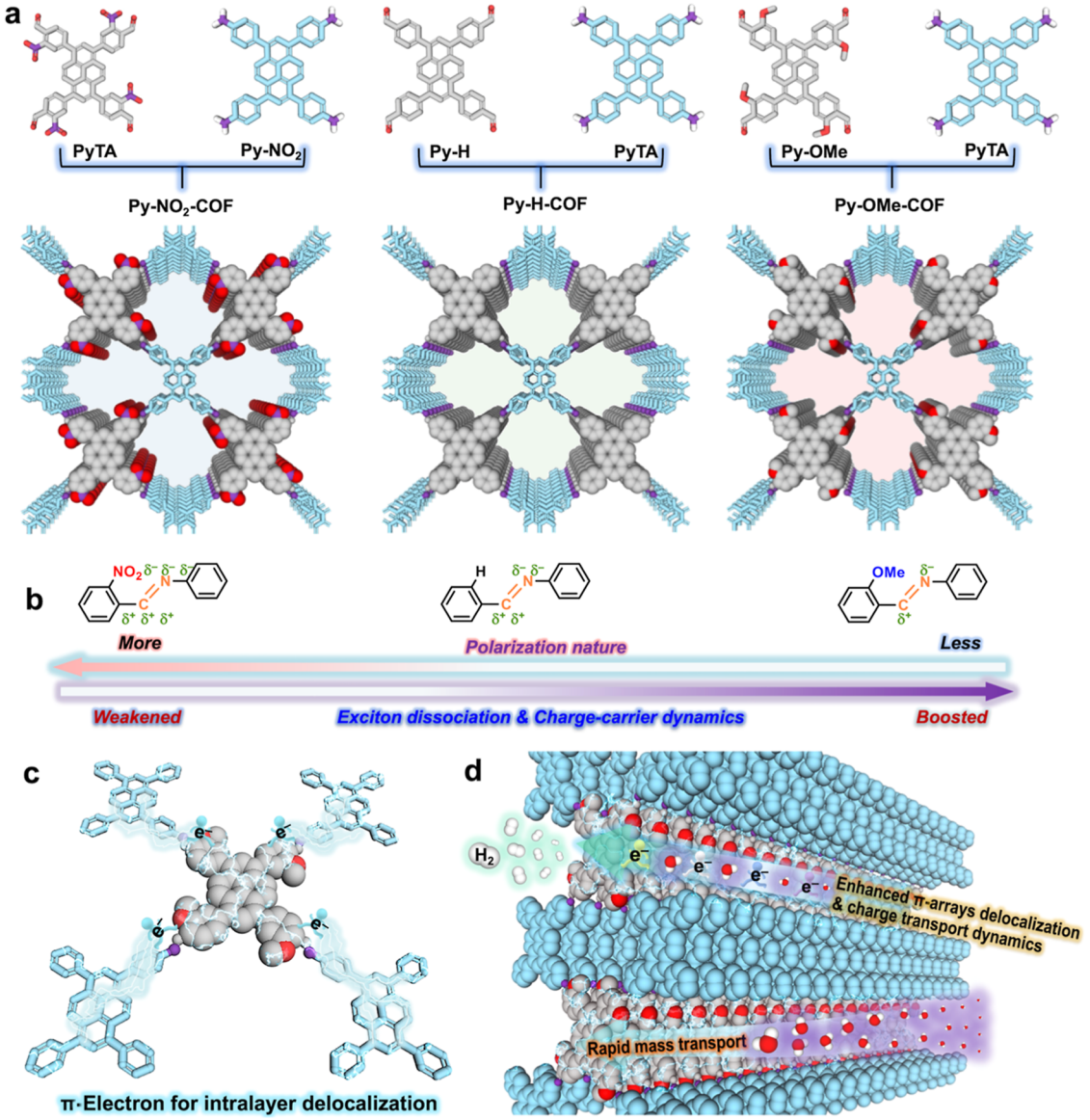

and severe charge recombination that compromises catalytic efficiency.[10]

Inspired by these competing effects, we hypothesized that strategically mitigating the polarization of imine linkages could restore extended π-conjugation and dramatically improve charge carrier dynamics, thereby boosting overall photocatalytic efficiency.[11] To validate this, we systematically investigated the effects of side-group functionalization on a series of pyrene-based tetragonal COFs (Py-R-COFs, R = −OMe, −H, $-NO_2$) (Chart 1a). Our central focus was to decode the complex interplay between structural polarization, π-electron delocalization, and charge transport kinetics.

Our findings demonstrate that decorating the COF pore walls with electron-donating methoxy (−OMe) substituents effectively attenuates C═N bond polarization and suppresses interlayer electrostatic repulsion (Chart 1b). This targeted modification yields multiple synergistic benefits for Py-OMe-COF: it enhances structural integrity and crystallinity, strengthens interlayer π−π interactions, and optimizes exciton dissociation to enable highly efficient intra- and inter-layer charge transfer (Chart 1c,d). Furthermore, the −OMe motifs anchor water molecules via hydrogen bonding, constructing an efficient pathway for proton transport (Chart 1d). As a result, Py-OMe-COF delivers an exceptional photocatalytic hydrogen evolution rate of ca. 100 mmol h^{-1} g_{cat}^{-1} and an apparent quantum yield (AQY) of 21.8 ± 0.80% at 450 nm, placing it among the highest-performing COF photocatalysts reported to date (Table S1). In stark contrast, introducing electron-withdrawing nitro ($-NO_2$) groups, exacerbated bond polarization and impaired π-stacking, leading to diminished photocatalytic activity despite establishing donor−acceptor (D−A) interactions. Collectively, this study provides microscopic insights and establishes a rational design principle for

https://doi.org/10.1021/jacs.6c04124
J. Am. Chem. Soc. XXXX, XXX, XXX−XXX

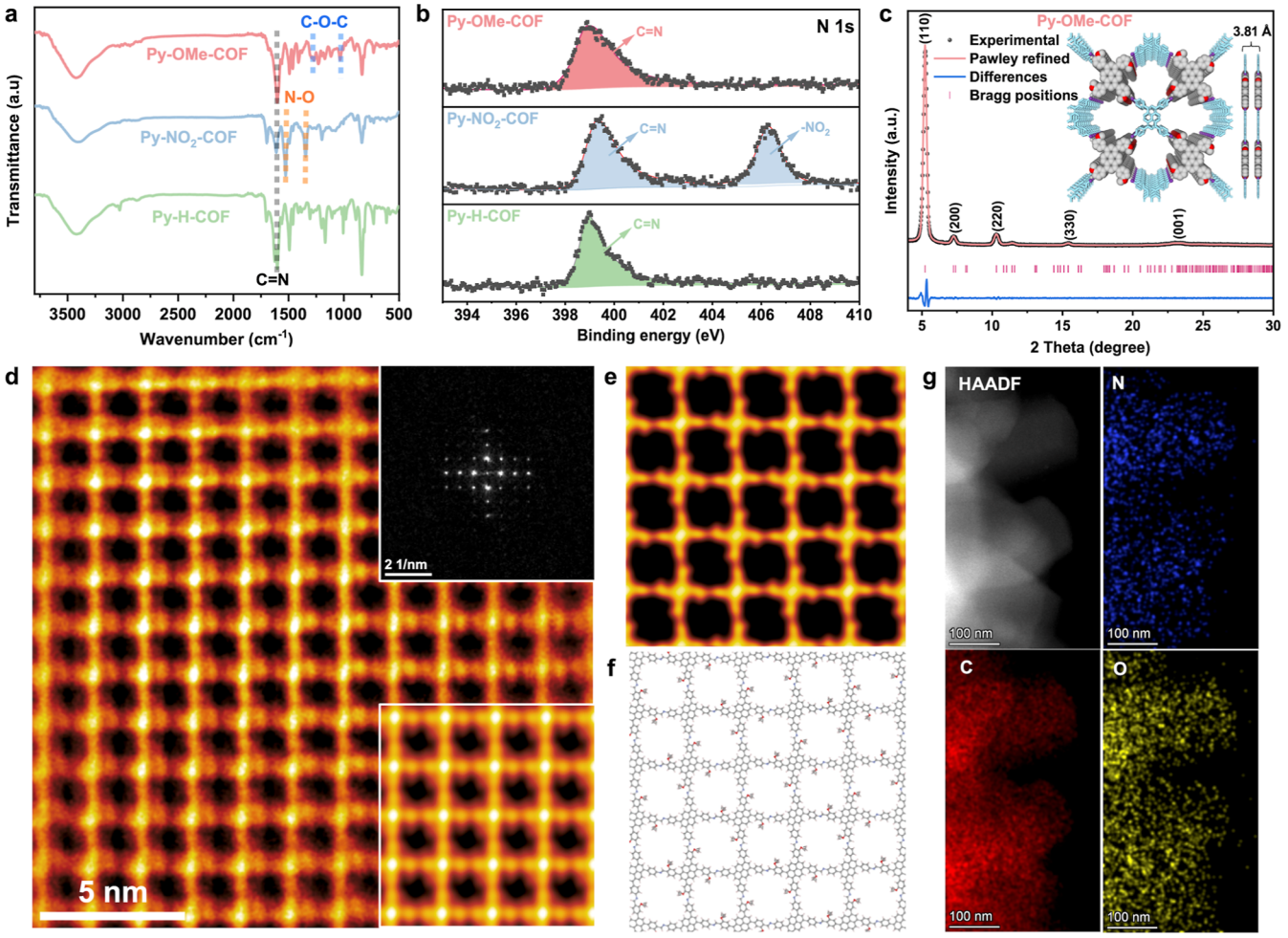

Figure 1. (a) FT-IR spectra of Py-R-COFs. (b) N 1s XPS profiles of Py-R-COFs. (c) Experimental and simulated PXRD patterns of Py-OMe-COF (atoms in the COF skeleton: carbon (gray); oxygen (red); nitrogen (purple); hydrogen was omitted). (d) Denoised and CTF-corrected HRTEM image of Py-OMe-COF acquired along the [001] zone axis (inset: FFT pattern (top-right), lattice-averaged image (bottom-right)). (e) Corresponding simulated projected electrostatic potential map. (f) Structural model. (g) Py-OMe−COF with elemental maps for C, N, and O.

engineering imine-linked COFs toward advanced solar-to-fuel conversion.

RESULTS AND DISCUSSIONS

Pyrene-based tetragonal COFs, Py-OMe−COF, Py-H−COF and Py-NO_2−COF, were synthesized through solvothermal polycondensations (Chart 1a) (for details see Experimental Section in the Supporting Information). The resulting frameworks, characterized by pyrene knots and linkers connected through imine bonds, exhibited distinct electronic and structural properties tailored by their side-group functionalities (−OMe, −H, and −NO_2).

Structural characterization was performed using Fourier-transform infrared (FT-IR) spectroscopy. The FT-IR spectrum exhibited the anticipated absence of aniline N−H stretching bands in the 3200−3400 cm^{-1} region, alongside the disappearance of carbonyl (C═O) vibration bands at approximately 1690 cm^{-1} (Figure S1). Characteristic C═N stretching vibrations were identified at ∼1620 cm^{-1}, while distinct signals corresponding to the functional moieties in Py-NO_2−COF (−NO_2: ∼1340, ∼1525 cm^{-1}) and Py-OMe−COF (−OMe: ∼1030, ∼1280 cm^{-1}) were also observe (Figure 1a).[12] X-ray photoelectron spectroscopy (XPS) corroborated these findings, revealing C═N peaks at ∼399 eV for all Py-R−COFs and a unique −NO_2 peak at ∼406 eV for Py-NO_2−COF[11a] (Figure 1b). Solid-state ^{13}C NMR spectroscopy further validated the incorporation of functional groups, identifying C═N (∼155 ppm) and −OMe (∼50 ppm) in Py-OMe−COF, and −NO_2 (∼189 ppm) in Py-NO_2−COF, while the signals in the range of 100−150 ppm were assigned to the sp^2-bonded carbon atoms of the framework (Figures S2−S4). XPS survey spectra (Figure S5) confirmed the presence of all expected elemental constituents. A minor oxygen signal detected in Py-H−COF is presumed to originate from adventitious adsorption of atmospheric water or molecular O_2. High-resolution XPS C 1s spectra indicated that electron-donating −OMe groups in Py-OMe−COF enhanced electron density at the imine carbons, evidenced by a negative shift relative to electron-withdrawing −NO_2 groups in Py-NO_2−COF,[13] mitigating imine linkage polarization and enhancing charge delocalization (Figure S6).

Powder X-ray diffraction (PXRD) analysis elucidated the crystallinity and interlayer interactions, with Py-OMe-COF displaying diffraction peaks at 2θ = 5.24°, 7.24°, 10.28°, 15.48°, and 23.50°, corresponding to the (110), (200), (220), (330), and (001) facets, respectively (Figure 1c). Py-NO_2−COF and Py-H−COF exhibited similar patterns with peaks at 2θ = 5.28°, 7.38°, 10.48°, 14.62°, 21.60° (Figure S7) and

https://doi.org/10.1021/jacs.6c04124
J. Am. Chem. Soc. XXXX, XXX, XXX−XXX

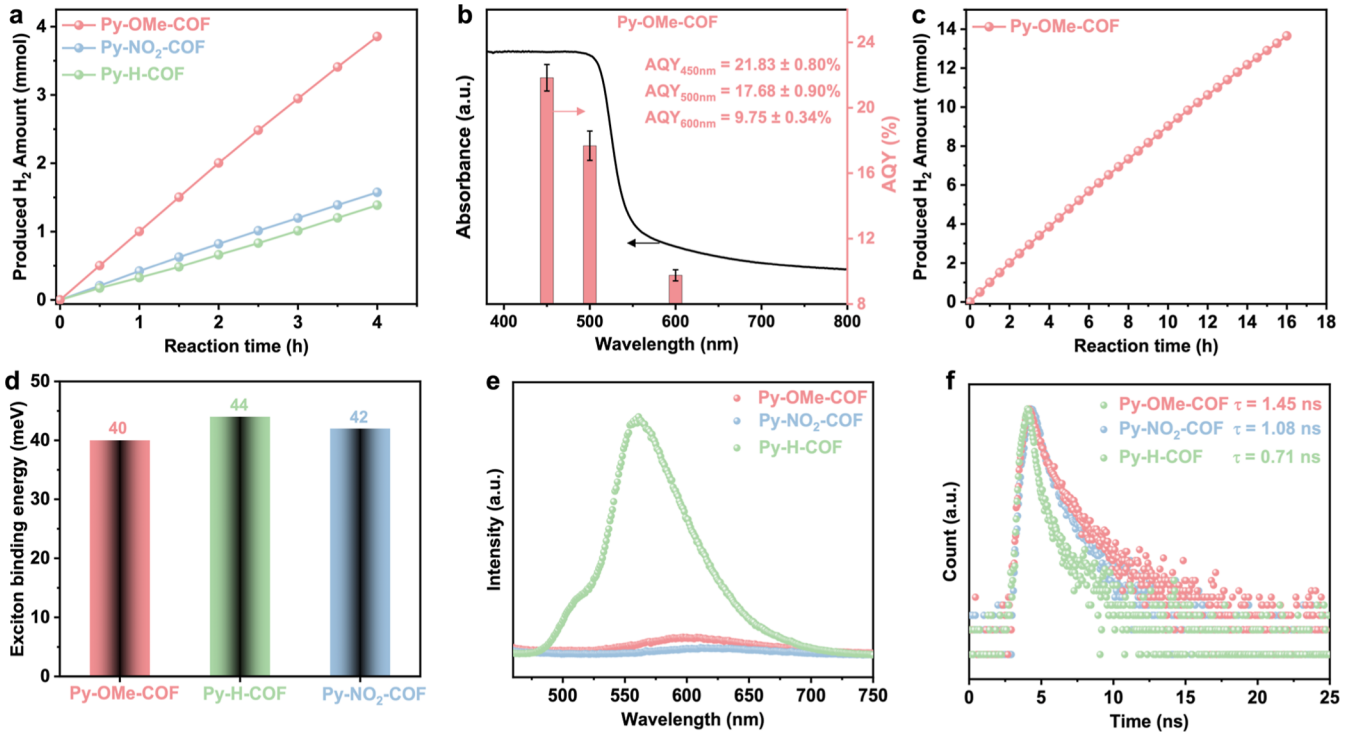

Figure 2. (a) Photocatalytic HER performances of Py-R−COFs. (b) The wavelength-dependent AQY of HER. (c) Stability and reusability H_2 evolution test employing Py-OMe−COF as a photocatalyst under visible light (λ > 420 nm) irradiation (evacuated each time after sampling). (d) The estimated exciton binding energy values, (e) steady-state PL spectra (λ_{ex} = 420 nm) and (f) PL decay spectra of the Py-R−COFs.

5.20°, 7.30°, 10.40°, 22.90° (Figure S8), respectively. Notably, the (001) peak shift to higher 2θ in Py-OMe−COF (23.50°) compared to Py-NO_2−COF (21.60°) and Py-H−COF (22.90°), suggesting stronger π−π interlayer interactions in Py-OMe−COF, likely due to enhanced electronic effects induced by the −OMe substituent. Furthermore, the full-width at half-maximum (fwhm) of the (110) peak was markedly narrower for Py-OMe−COF (0.301°) compared to Py-NO_2−COF (0.409°) and Py-H−COF (0.538°), indicating superior crystallinity in Py-OMe−COF. These findings suggest that the −OMe substitution enhances the stability of C═N bonds, thereby promoting stronger interlayer π−π interactions and greater π-electron delocalization. Additionally, simulated PXRD patterns confirmed eclipsed (AA) stacking for all COFs, aligning with experimental data (Figures S9−S12). The associated refinement residuals were determined to be R_{wp} = 7.25%, R_p = 5.30% for Py-OMe−COF; R_{wp} = 6.73%, R_p = 5.08% for Py-NO_2−COF; R_{wp} = 7.72%, R_p = 5.62% for Py-H−COF (Table S2).

Morphological analysis via field emission scanning electron microscopy (FE-SEM) revealed rectangular-like particles for Py-OMe−COF, aggregated structures for Py-NO_2−COF, and rod-like morphologies for Py-H−COF (Figures S13−S15), with Py-OMe−COF's ordered morphology likely enhancing active site accessibility for photocatalysis. The recent advancement of low-dose electron microscopy techniques enables the direct visualization of real-space atomic structures of beam-sensitive materials such as COFs.[14] Utilizing this technique, we successfully achieved high-resolution imaging of Py-R−COF crystals. As illustrated in Figure 1d, a low-dose high-resolution transmission electron microscopy (HRTEM) image of Py-OMe−COF was acquired along the [001] zone axis. Following denoising and correction of the contrast reversal effects induced by the objective lens (CTF correction), the image clearly reveals a tetragonally arranged structure with an ordered symmetry. In this structure, the pyrene units are positioned at the four vertices of the unit cell, manifested as bright contrast features, and are interconnected via imine linkages, which appear as the bright short edges of the closed square framework. The methoxy groups are situated on one side of these short edges, exhibiting darker contrast. The Fast Fourier Transform (FFT) pattern in the inset (top-right, Figure 1d) displays sharp diffraction spots with distinct 4-fold symmetry, confirming the high crystallinity of the material. The crystal structure is more clearly visualized through the lattice-averaged image (bottom-right inset, Figure 1d), a method that effectively and simultaneously eliminates the impacts of residual aberrations, zone axis misalignment, and high noise levels. Furthermore, the observed 4-fold symmetric lattice network shows excellent agreement with the simulated projected electrostatic potential and the structural model of the 2D Py-OMe−COF crystal (Figure 1e,f). Elemental mapping further validates the chemical composition of the proposed structure, revealing a uniform spatial distribution of C, N, and O elements within the Py-OMe−COF (Figure 1g). Similarly, chemically interpretable high-resolution images were obtained for the 2D networks of Py-NO_2−COF and Py-H−COF, which are in good consistency with the simulated 2D crystal structures and projected electrostatic potentials (Figures S16 and S17). The uniform distribution of C, N, and O in Py-NO_2−COF, along with C and N in Py-H−COF, further confirms the chemical composition of these framework materials (Figures S18 and S19). Nitrogen sorption at 77 K yielded Brunauer−Emmett−Teller (BET) surface areas of 1249, 1061, and 414 $m^2\ g^{-1}$ for Py-OMe−COF, Py-H−COF, and Py-NO_2−COF, respectively (Figure S20), with Py-OMe−

https://doi.org/10.1021/jacs.6c04124
J. Am. Chem. Soc. XXXX, XXX, XXX−XXX

COF's highest surface area reflecting its superior structural order. Quenched solid density functional theory (QSDFT) pore size analysis indicated micropores of 1.56 nm (Py-OMe−COF), 1.45 nm (Py-NO_2−COF), and 1.61 nm (Py-H−COF) (Figure S21), consistent with TEM observations.[15]

UV−vis diffuse reflectance spectroscopy (DRS) were employed to evaluate the light-harvesting ability of Py-R−COFs, revealing strong absorption band at ca. 500 nm, indicative of their visible-light responsiveness (Figure S22a). The optical bandgaps (E_g) were determined as 2.31 eV (Py-OMe−COF), 2.10 eV (Py-NO_2−COF), and 2.36 eV (Py-H−COF) (Figure S22b), with narrower bandgaps in Py-OMe−COF and Py-NO_2−COF attributed to p-π resonance from −OMe lone pairs and electron push−pull effects from $-NO_2$ substituents, respectively. Mott−Schottky analysis was subsequently performed to ascertain the flat-band potentials. Given the n-type semiconducting character of these materials, the conduction band edge (E_{CB}) is approximated by the flat-band potential derived from the Mott−Schottky plots (Figure S23). The resulting E_{CB} values (vs. NHE) are −0.80 V for Py-OMe−COF, −0.75 V for Py-NO_2−COF, and −0.55 V for Py-H−COF, indicating that Py-OMe−COF possesses the most favorable thermodynamic driving force for the hydrogen evolution reaction (HER). The valence band (E_{VB}) was then calculated using the relationship $E_g = E_{VB} - E_{CB}$, and the corresponding energy band diagrams were constructed accordingly (Figure S24).

The stability of the Py-R−COFs under pertinent operating conditions is essential for their prospective application in photocatalysis. Accordingly, both the thermal robustness and chemical resilience of the materials were systematically evaluated. Thermogravimetric analysis (TGA) (Figure S25a) conducted under a nitrogen atmosphere demonstrates that all three COFs exhibit high thermal stability up to 300 °C. Chemical stability was further probed by immersing the COFs in a range of solvents and aggressive media—including tetrahydrofuran (THF), water (H_2O), dichloromethane (DCM), N,N-dimethylformamide (DMF), 12 M HCl, and 12 M NaOH—for a duration of 24 h. Post-treatment PXRD patterns (Figure S25b,d) confirm the retention of crystallinity for all three frameworks, thereby substantiating their chemical integrity even under strongly acidic and basic conditions. This pronounced chemical resilience is particularly advantageous for photocatalytic processes that frequently necessitate operation in extreme pH environments.

Photocatalytic HER performance was initially evaluated using 3 wt % Pt (actual loading: 0.60−0.73 wt %, Table S3) as a cocatalyst and ascorbic acid (AC) as a sacrificial electron donor (SED) under visible-light radiation (λ > 420 nm). Py-OMe−COF (10 mg) exhibited an exceptional HER rate of ca. 100 mmol h^{-1} g_{cat}^{-1} (Figure S26), significantly outperforming Py-NO_2−COF and Py-H−COF (Figure 2a). A systematic evaluation of alternative sacrificial agents—including methanol (MeOH), sodium ascorbate (SA), AC, and triethanolamine (TEOA)—identified AC as the most efficacious electron donor (Figure S27). Subsequent optimization of both the Pt loading and the photocatalyst mass for Py-OMe−COF (Figure S28) established that the combination of 10 mg of photocatalyst and 3 wt % Pt cocatalyst, with AC serving as the SED, affords the maximum HER activity. Under these optimized conditions, apparent quantum yield (AQY) measurements were performed. AQYs for Py-OMe−COF were 21.83 ± 0.80%, 17.68 ± 0.90%, and 9.75 ± 0.34% at 450, 500, and 600 nm, respectively (Figure 2b), correlating closely with its UV−vis DRS profile and highlighting its superior light-harvesting capability. Notably, the AQY value of Py-OMe−COF at 450 nm (AQY_{450nm} = 21.83 ± 0.80%) surpasses most previously reported COF-based photocatalytic systems for HER (Table S1), underscoring the effectiveness of the −OMe functionalization strategy. The durability of Py-OMe−COF was further assessed through three consecutive cycling tests (3 × 5 h) and an extended 16 h experiment. As shown in Figures S29 and 2c, Py-OMe-COF sustained robust photocatalytic performance throughout both series of measurements. Postreaction characterization by FT-IR, PXRD, and SEM analyses verifying structural integrity (Figures S30−S32).

To exclude the possibility that the superior HER activity of Py-OMe−COF arises from variations in actual Pt loading (Figure S33) or BET surface area (Figure S34), a series of control experiments were conducted. With respect to Pt loading, inductively coupled plasma (ICP) analysis indicated that even when Py-NO_2−COF was loaded with a comparable actual Pt content (0.75 wt % at a nominal loading of 5 wt %) to that of Py-OMe−COF (0.73 wt % at a nominal loading of 3 wt %) (Table S3), its HER activity remained substantially inferior (343 vs 982 μmol h^{-1}). Moreover, experiments performed in the absence of Pt cocatalyst revealed that Py-OMe−COF still exhibited markedly higher activity than both Py-H−COF and Py-NO_2−COF. Regarding surface area effects, additional control experiments were performed by optimizing the synthesis and activation conditions of Py-NO_2−COF to enhance its porosity from 414 to 1205 m^2 g^{-1}. This increase in surface area, however, led to only a marginal improvement in HER activity, indicating that BET surface area alone does not constitute the predominant factor governing photocatalytic performance. Collectively, these findings substantiate that the enhanced photocatalytic performance of Py-OMe−COF is primarily attributable to the attenuation of imine bond polarization imparted by the electron-donating methoxy substituents, rather than to disparities in Pt loading or BET surface area.

Given the appropriate band alignment of Py-R−COFs (Figure S24), their photocatalytic performance toward the oxygen evolution reaction (OER) was evaluated (Figure S35). OER measurements were carried out under visible-light irradiation with Py-R−COFs serving as the photocatalyst, in the presence of 3 wt % Co-based cocatalyst and $AgNO_3$ as the sacrificial electron acceptor. Among the series, Py-OMe−COF exhibits the highest OER activity, achieving an oxygen evolution amount of ca. 12 μmol over 4 h under visible-light irradiation. This observation suggests that further structural optimization of Py-OMe−COF could render it a promising candidate for overall water splitting applications.

To elucidate the photophysical mechanisms driving the superior photocatalytic performance of Py-OMe−COF, comprehensive characterizations were conducted. Exciton binding energy (E_b), critical for assessing electron−hole pair recombination and separation efficiency, was determined via temperature-dependent photoluminescence (PL) measurements from 15 to 300 K.[4b,d,15] Notably, Py-OMe−COF exhibited the lowest E_b (~40 meV) compared to Py-NO_2−COF (~42 meV) and Py-H−COF (~44 meV), indicating enhanced exciton dissociation, which facilitates efficient charge separation and contributes to its highest photocatalytic performance (Figures 2d and S36). Steady-state PL spectra showed that the emission intensity significantly decreased from

https://doi.org/10.1021/jacs.6c04124
J. Am. Chem. Soc. XXXX, XXX, XXX−XXX

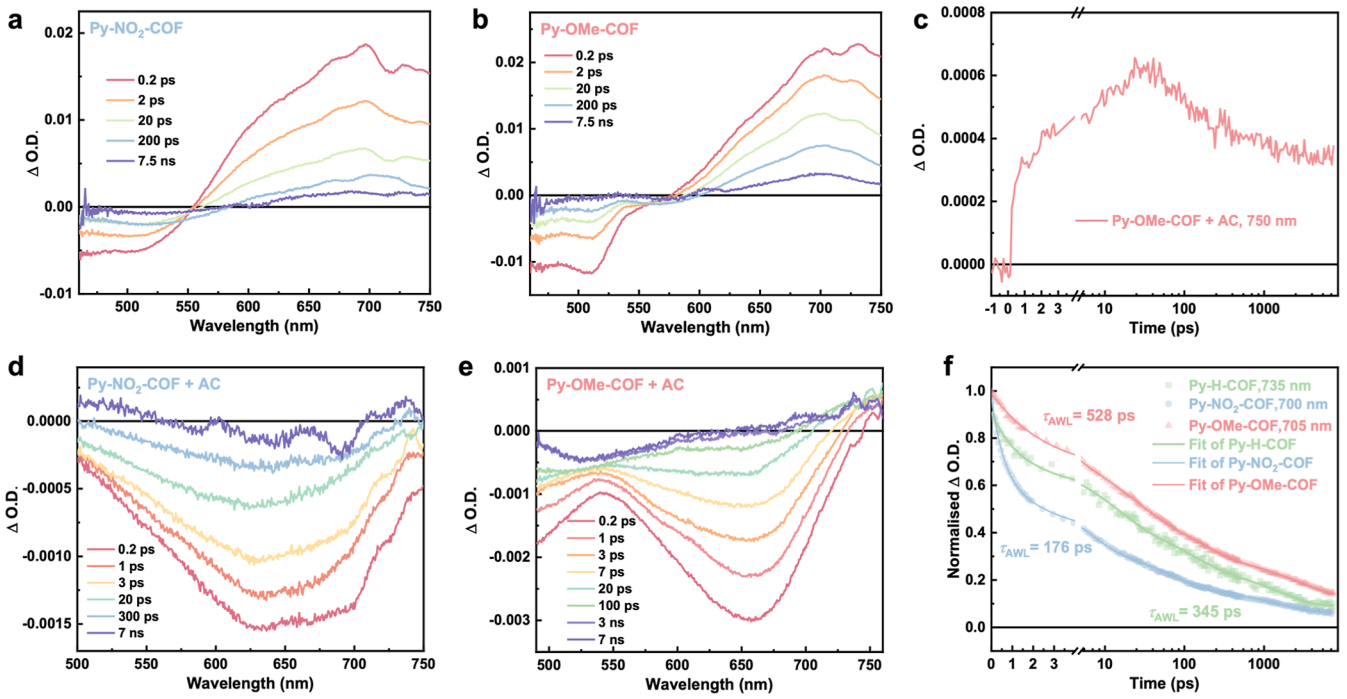

Figure 3. (a,d) TA spectra of Py-NO_2−COF in the absence and presence of ascorbic acid (0.1 M) following 435 nm excitation probed at selected time delays. (b,e) Transient absorption spectra of Py-OMe−COF in the absence and presence of ascorbic acid (0.1 M) following 435 nm excitation probed at selected time delays. (c) Kinetics of photoinduced absorption probed at 750 nm for Py-OMe−COF in the presence of ascorbic acid. (f) Normalized kinetic traces of photoinduced absorption bands at their maximum for Py-R−COFs.

Py-H−COF to Py-NO_2−COF, with Py-OMe−COF's intensity comparable to that of Py-NO_2−COF despite lacking D−A interactions, suggesting suppressed charge recombination due to −OMe group electron donation (Figure 2e). Time-correlated single photon counting (TCSPC) profiles revealed a prolonged charge carrier lifetime for Py-OMe−COF (1.45 ns) compared to Py-H−COF (1.08 ns) and Py-NO_2−COF (0.71 ns), showing the enhanced charge separation efficiency in Py-OMe−COF (Figure 2f). All these attributes collectively contribute to the remarkable photocatalytic performance of Py-OMe−COF, underscoring the effectiveness of −OMe functionalization in tailoring the electronic structure and enhancing photocatalytic performance.

To further elucidate the charge carrier kinetics of these COFs, femtosecond transient absorption (fs-TA) UV−vis spectroscopic measurements were conducted (Figures 3 and S37−S38). Compared to COF-suspended solutions, photo-excitation of thin-film COF samples (prepared as detailed in the Supporting Information) generate more reliable TA data under low-scattering conditions.

Upon excitation at 435 nm, fs-TA spectra of Py-NO_2−COF exhibited a broad photoinduced absorption (PIA) band spanning 550−750 nm and a negative band below 550 nm (Figure 3a). This spectral feature closely resembles those reported for other COFs.[16] The negative signal corresponds to ground state bleach (GSB) of the band edges, consistent with the inverse of the ground-state UV−vis DRS. Based on prior studies of COFs, the PIA band was assigned to photogenerated holes, also as evidenced by the nearly parallel kinetics of rapid GSB recovery and PIA band decay (Figures 3f and S39).[16c] The TA spectral features of Py-H−COF are similar to that of Py-NO_2−COF (Figure S37), showing a GSB band below 625 nm and a broad PIA band >625 nm. In contrast, Py-OMe−COF distinctly exhibited two negative bands: a dominant GSB at 520 nm (within ∼1 ps) and a weak stimulated emission (SE) between 540−600 nm appearing later (∼200 ps−7.5 ns) (Figure 3b). This SE feature aligns well with the observed emission lifetime (1.45 ns) from TCSPC measurements (Figure 2f). Divergent recovery kinetics of the GSB (505 nm) and the PIA band (700 nm) decay in Py-OMe−COF, unlike Py-NO_2−COF (Figures 3f and S39), suggested more complex excited-state dynamics influenced by the electron-donating −OMe substituents.

To study the intricate excited-state behaviors of these COFs, ascorbic acid was introduced as a hole acceptor, which significantly altered their fs-TA spectral profiles (Figures 3d,e and S38). In Py-NO_2−COF, ascorbic acid fully quenched the PIA band, producing a broad negative feature at ∼650 nm (Figure 3d), confirming efficient electron scavenging and the assignment of the PIA (>560 nm) to free photogenerated holes (Figure 3a). For Py-OMe−COF, a new positive band emerged at ∼540 nm within 0.2 ps, overlapping GSB and SE bands, and accompanied by a minor PIA tail near 750 nm (Figure 3e). Within ∼20 ps, this short-wavelength PIA progressively decayed, while a long-wavelength PIA (>650 nm) developed, indicating trapped electron/polaron formation from photo-generated free electrons at 540 nm following rapid hole capture by ascorbic acid within the instrumental response time (Figures 3c,e and S40). Subsequent slow electron−hole recombination process led to the decay of the trapped electron signal and the growth of a broad negative absorption band at ∼525 nm assigned to GSB simultaneously (Figure 3e). In comparison, Py-H−COF showed similar positive band (∼550 nm) assigned to free electrons at the initial ps time scale in the presence of SED; however, this feature decayed rapidly, and no long-lived polarons were observed (Figure S38).

Quantitative TA kinetics analyses of these COFs (Figure 3f) revealed extended charge carrier lifetimes for Py-OMe−COF

https://doi.org/10.1021/jacs.6c04124
J. Am. Chem. Soc. XXXX, XXX, XXX−XXX

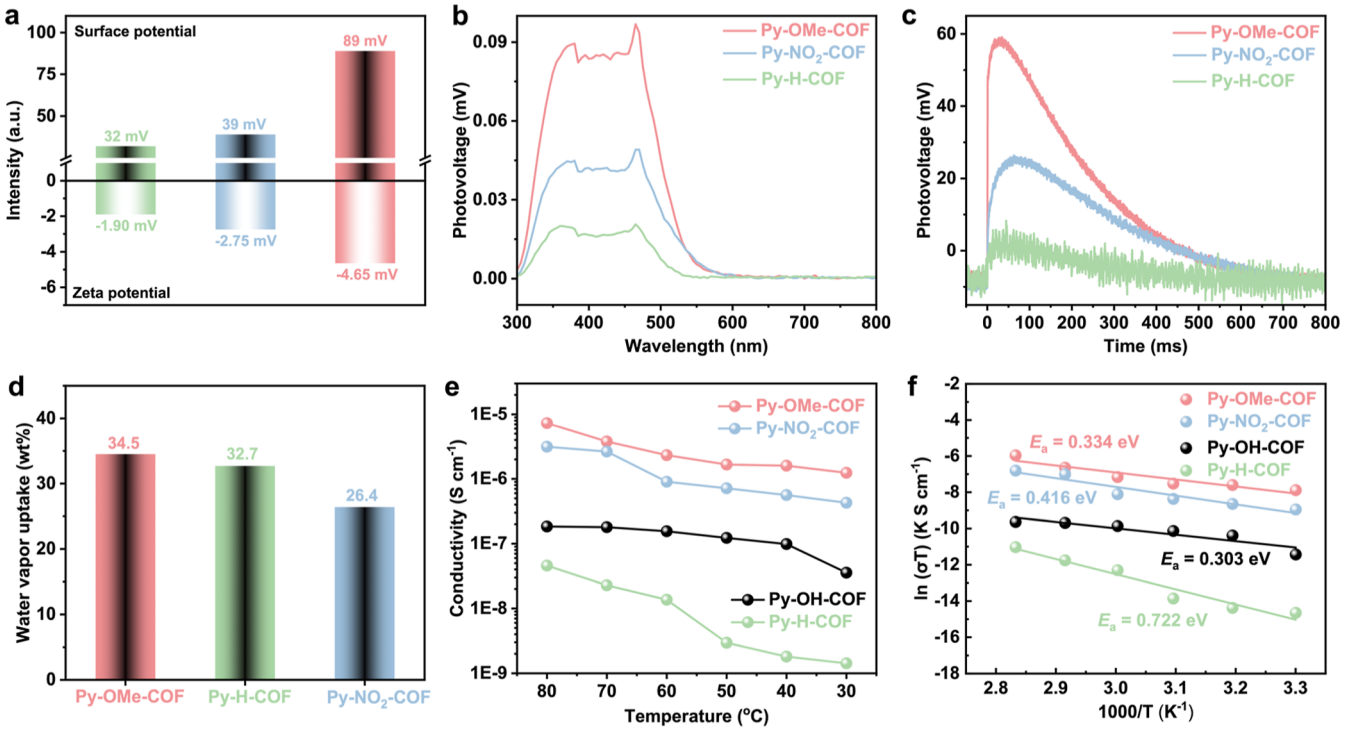

Figure 4. (a) Surficial electrostatic potential and Zeta potential (Py-H−COF (green); Py-NO_2−COF (blue); Py-OMe−COF (red)). (b) Steady-state surface photovoltage spectroscopy results. (c) Transient-state surface photovoltage spectra. (d) Water vapor uptake capacity of Py-R−COFs. (e) Proton conductivities (σ, from 353 to 303 K at 98% RH). (f) Arrhenius plots (under 98% RH) of Py-R−COFs.

(528 ps) compared to Py-NO_2−COF (176 ps) and Py-H−COF (345 ps), demonstrating effectively suppressed electron−hole recombination. Notably, distinct long-lived signals corresponding to trapped electrons were exclusively detected in Py-OMe−COF upon hole scavenging with ascorbic acid (Figure 3c). These findings illustrate that electron-donating −OMe substituents effectively mitigate imine bond polarization through p-π electron modulation, thereby prolonging charge carrier lifetimes and substantially enhancing photocatalytic HER efficiency.

Photoelectrochemical experiments further elucidated charge migration behaviors under light irradiation. Transient photocurrent measurements revealed markedly enhanced transient photocurrent for Py-OMe−COF (Figure S41), reflecting efficient charge carrier separation and migration due to alleviated imine polarization. In contrast, Py-NO_2−COF and Py-H−COF showed minimal photocurrent variation, likely due to exacerbated polarization of the imine linkage hindering π-electron delocalization and charge transport. Electrochemical impedance spectroscopy (EIS) analysis (Figure S42) further corroborated these findings, demonstrating that Py-OMe-COF consistently displays the smallest semicircular radius in the Nyquist plots irrespective of illumination status. This observation signifies superior charge carrier transport efficiency and substantially reduced interfacial charge-transfer resistance relative to the other COF analogues.

Kelvin probe force microscopy (KPFM) was employed to elucidate the surface charge separation and transfer kinetics in Py-R−COFs. Notably, Py-OMe−COF presented a markedly higher surficial electrostatic potential compared to Py-NO_2−COF and Py-H−COF (Figures 4a and S43−S45). Additionally, Zeta potential measurements revealed values of −4.65 mV, −2.75 mV, and −1.90 mV for Py-OMe−COF, Py-NO_2−COF, and Py-H−COF, respectively (Figures 4a and S46). A positive correlation was observed between the intensity of the built-in electric field and both the surface potential and Zeta potential of Py-R−COFs, consistent with previous studies.[15a,17] These findings indicate that modulation of the polarization effect of imine linkages can enhance the built-in electric field, thereby facilitating the transfer of photoexcited charge carriers from the particle surface to reactants and improving interfacial charge transfer dynamics.

To further investigate surface charge separation and transfer processes, surface photovoltage spectroscopy (SPV) and transient-state surface photovoltage (TPV) measurements were conducted.[18] The SPV results demonstrated that Py-OMe−COF exhibited a significantly stronger steady-state SPV intensity, indicative of enhanced migration of photogenerated carriers from the bulk to the surface of the photocatalyst surface (Figure 4b). Similarly, TPV measurements revealed a substantially accelerated generation of photogenerated charges in Py-OMe−COF upon light illumination (Figure 4c). These photoelectrochemical and photophysical observations, which align closely with the KPFM results, collectively underscore the strategy of modulating the polarization of imine-linked COFs by incorporating electron-donating −OMe groups to enhance charge separation and migration efficiency.

To clarify the interplay between proton conduction and photocatalytic HER activity, the proton transport behavior was systematically investigated in these COFs, given its established critical role in photocatalytic HER processes.[19] Proton conductivity was assessed using Nyquist plot measurements conducted at 98% relative humidity (RH) across from 303 to 353 K (Figures S47−S49). Py-OMe−COF exhibited the lowest surface impedance, followed by Py-H−COF and Py-NO_2−COF, a trend that closely corresponded to their relative hydrophilicities, as substantiated by water contact angle measurements (35.0° for Py-OMe−COF, 39.6° for Py-H−

https://doi.org/10.1021/jacs.6c04124
J. Am. Chem. Soc. XXXX, XXX, XXX−XXX

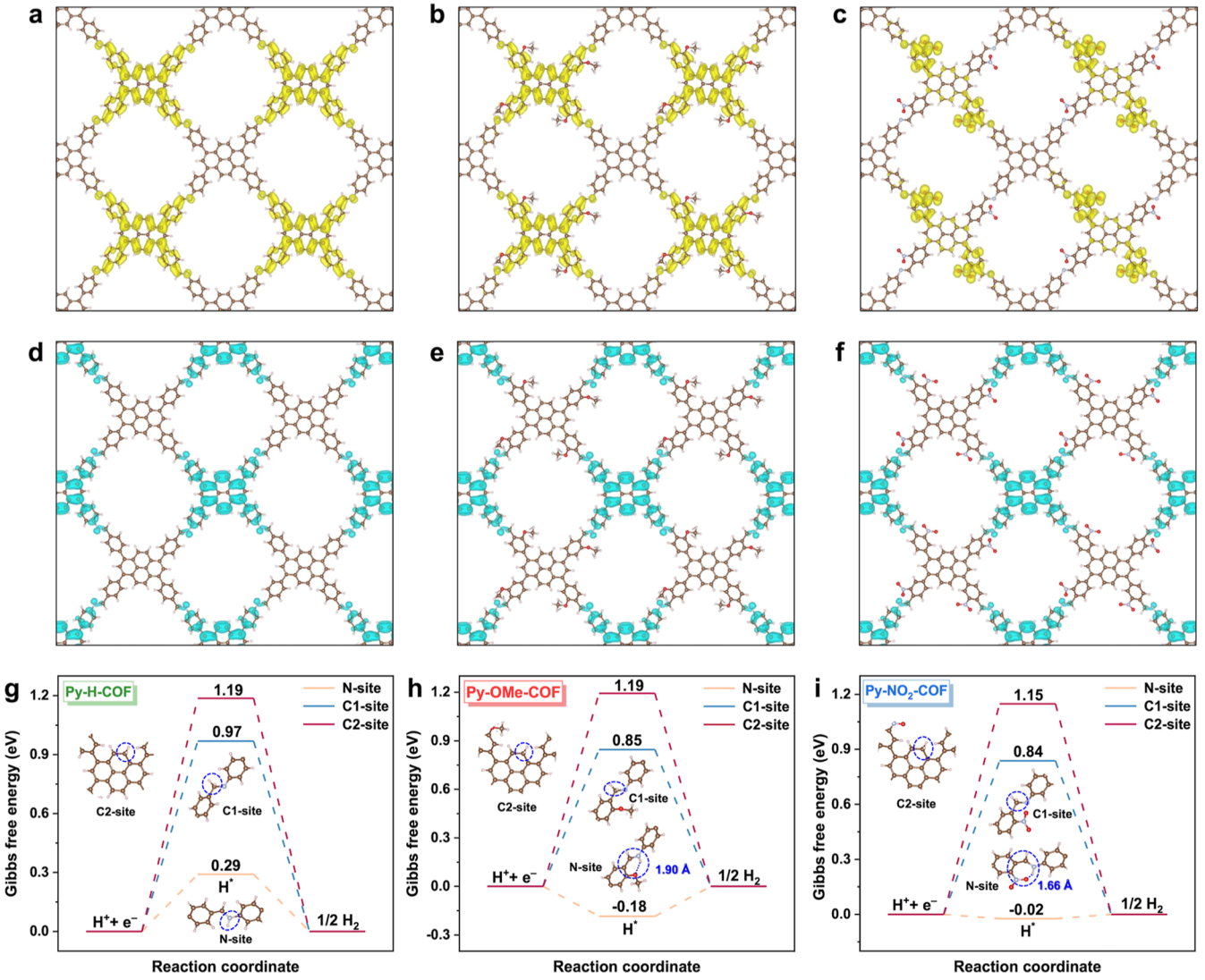

Figure 5. CBM of (a) Py-H−COF, (b) Py-OMe−COF, (c) Py-NO_2−COF. The VBM of (d) Py-H−COF, (e) Py-OMe−COF, (f) Py-NO_2−COF. Gibbs free energy diagrams of (g) Py-H−COF, (h) Py-OMe−COF, (i) Py-NO_2−COF.

COF, and 40.3° for Py-NO_2−COF) (Figure S50) and water vapor uptake experiments (Figures 4d and S51). The proton conductivities (σ) at 303 K and 98% RH were determined to be 1.24×10^{-6} S cm^{-1}, 1.43×10^{-9} S cm^{-1}, and 4.26×10^{-7} S cm^{-1} for Py-OMe−COF, Py-H−COF, and Py-NO_2−COF, respectively (Figure 4e).

The activation energy (E_a) for proton transport of these COFs was calculated to further probe the underlying mechanisms (Figure 4f). Py-OMe−COF exhibited the lowest E_a (0.334 eV), consistent with the Grötthuss proton-hopping mechanism ($E_a \leq 0.40$ eV), which is facilitated by an ordered hydrogen-bonded network. In contrast, Py-H−COF (0.722 eV) and Py-NO_2−COF (0.416 eV) displayed higher E_a values, indicative of proton conduction dominated by the vehicle mechanism ($E_a > 0.4$ eV), characterized by the diffusion of protonated species.[20] The low E_a of Py-OMe−COF suggests that its ordered pore channels enable low-energy transitions within the proton conduction network, creating an optimal environment for efficient proton transport.

To further validate the proposed role of the −OMe in establishing an ordered hydrogen-bond network and to decouple its hydrogen-bonding contribution from purely electronic effects, a hydroxyl-functionalized COF analogue (Py-OH-COF) was synthesized. The successful formation of Py-OH-COF was verified by solid-state ^{13}C NMR spectroscopy (Figure S52a), FT-IR spectroscopy (Figure S52b), and PXRD (Figure S53). Proton conductivity measurements conducted at 303 K and 98% RH revealed that Py-OH-COF (Figure S54) exhibits a conductivity of 3.56×10^{-8} S cm^{-1} (Figure 4e), which is markedly lower than that of Py-OMe-COF (1.24×10^{-6} S cm^{-1}). The E_a for proton transport in Py-OH-COF was determined to be 0.304 eV (Figure 4f), a value consistent with the Grotthuss mechanism ($E_a \leq 0.40$ eV) and indicative of the presence of an ordered hydrogen-bond network. Evaluation of photocatalytic HER activity yielded a rate of 441 μmol h^{-1} for Py-OH-COF (Figure S55), substantially inferior to that of Py-OMe-COF (ca. 1 mmol h^{-1}). These results suggest that while −OH group is capable of participating in hydrogen bonding, resulting proton conductivity and HER performance are significantly lower than those afforded by the methoxy group, thereby underscoring the distinctive advantage conferred by the −OMe substituent.

To directly interrogate hydrogen-bonding interactions, in situ variable-temperature FT-IR spectroscopy was performed

https://doi.org/10.1021/jacs.6c04124
J. Am. Chem. Soc. XXXX, XXX, XXX−XXX

on Py-H−COF, Py-NO_2−COF, Py-OMe−COF, and Py-OH−COF across the temperature range of 298−393 K (Figures S56 and S57). The spectrum of Py-H−COF is characterized by broad O−H stretching bands spanning 3100−3600 cm^{-1} and an N−H vibrational feature centered at ∼3360 cm^{-1}. In the case of Py-NO_2−COF, a distinct peak corresponding to free water is observed at ∼3650 cm^{-1}, accompanied by the N−H signal at ∼3360 cm^{-1} and additional contributions attributable to water molecules hydrogen-bonded to oxygen (3460 cm^{-1}) and nitrogen (3550 cm^{-1}) sites.[21] Py-OMe−COF and Py-OH−COF exhibit qualitatively similar spectral features; however, they are distinguished by prominent hydrogen-bonding signatures at 3220 and 3130 cm^{-1}, which are indicative of strong interactions between the hydrophilic functional groups and adsorbed water molecules.[22] Such strong hydrogen-bonding interactions are conducive to efficient proton transfer between donor and acceptor moieties, thereby facilitating proton transport via the Grotthuss mechanism.

To quantitatively assess the strength of hydrogen-bonding interactions, the O−H stretching region (3000−3800 cm^{-1}) was deconvoluted into three distinct spectral components: network water (NW, corresponding to strongly hydrogen-bonded water), intermediate water (IW, associated with distorted hydrogen bonds), and multimeric water (MW, attributed to weakly bound or free water). The proportion of NW was found to increase in the following order: Py-H−COF (24%) < Py-NO_2−COF (35%) < Py-OH−COF (39%) < Py-OMe−COF (41%) (Figure S58).[23] This trend provides direct evidence that Py-OMe−COF sustains the most extensive and robust hydrogen-bond network among the investigated materials, thereby rationalizing its superior proton conductivity and enhanced HER performance. Collectively, these results furnish direct experimental validation that the methoxy substituent plays a pivotal role in establishing a durable hydrogen-bond network that facilitates efficient proton transport.

The exceptional proton conductivity of Py-OMe−COF can be attributed to its abundant hydrophilic −OMe groups, which establish a dense hydrogen-bonding network between oxygen species in the pore walls and adsorbed water molecules. This network supports the Grötthuss mechanism, allowing efficient proton hopping efficiently through interconnected hydrogen bonds. Furthermore, the enriched proton population around the −OMe groups may facilitate rapid transfer to adjacent reduction sites, thereby accelerating proton reduction reactions. These findings underscore the critical role of incorporating electron-donating methoxy groups in enhancing both electron transfer and proton transport while suppressing electron−hole recombination. Collectively, these attributes synergistically drive the superior photocatalytic HER performance of Py-OMe−COF, highlighting the strategic value of functional group engineering in optimizing the performance of COFs for photocatalytic applications.

To elucidate the microscopic mechanism of the photocatalytic HER in these COFs, density functional theory (DFT) calculations were conducted to provide theoretical insights into the charge transfer and reaction dynamics. Analysis of the spatial charge density distribution, specifically the valence band maximum (VBM) and conduction band minimum (CBM), reveals a pronounced spatial separation in the Py-R−COF configurations (Figure 5a−f). These structural attributes were found to be conducive to efficient photoinduced charge separation. Notably, the Py-NO_2−COF exhibits a typical D−A charge separation structure (Figure 5c,f), with charge density predominantly localized at the nitro units.

DFT calculations further revealed that the −OMe moieties in Py-OMe−COF serve as preferential sites for concentrating both H_2O molecules and protons, thereby substantiating their involvement in photochemical reactions. Furthermore, the adsorption energies for both H_2O adsorption models on Py-OMe−COF (E_{ads} = −0.50 eV) were found to be more favorable than those for Py-H−COF (E_{ads} = −0.43 eV) and Py-NO_2−COF (E_{ads} = −0.34 eV) (Figure S59). This suggests that the −OMe units in Py-OMe−COF act as effective proton extractors, potentially accelerating proton transfer and enhancing mass transport kinetics. These results align with experimental proton conduction measurements, indicating that photogenerated carriers on the photocatalyst surfaces engage in proton-coupled reactions with activated protons, thereby promoting the photocatalytic process.

To attain a more comprehensive understanding of the electronic perturbations induced by the substituents, DFT calculations were undertaken to map the electrostatic potential (ESP) distributions across the three COF frameworks (Figure S60). The imine moieties in Py-OMe−COF exhibit an enhanced electron density relative to those in Py-H−COF, attributable to the p-π conjugation imparted by the electron-donating methoxy substituents. Conversely, the incorporation of electron-withdrawing nitro groups in Py-NO_2−COF renders the imine linkages comparatively electron-deficient, thereby exacerbating bond polarization. These results substantiate that −OMe substitution effectively mitigates the inherent polarization of the C═N bonds within the framework.

Furthermore, to theoretically elucidate the formation of the hydrogen-bonding network, we evaluated the interactions between the COF frameworks and water molecules (Figure S61). The results show that Py-OMe−COF forms more abundant and stronger O−H···O and O−H···N hydrogen bonds with water compared to Py-NO_2−COF and Py-H−COF, indicating enhanced water affinity and a greater propensity for constructing an extended hydrogen-bond network. These findings are consistent with the experimental observations from in situ variable-temperature FT-IR spectroscopy (Figures S56 and S57) as well as the calculated water adsorption energies (Figure S59). Collectively, the DFT results provide compelling evidence for both the attenuation of imine bond polarization and the establishment of an extensive hydrogen-bonding network in Py-OMe−COF. These synergistic effects are conducive to efficient charge separation and proton transport within the framework.

To quantitatively assess the steric influence of substituents on the framework geometry, DFT calculations were further performed to determine the dihedral angles within the Py-R-COF structures (Figures S62−S64). In Py-H−COF, the imine unit exhibits a dihedral angle of 18.59°, while the pyrene moieties display dihedral angles of 42.75° and 44.15°. Upon incorporation of methoxy groups, Py-OMe−COF shows imine dihedral angles of 21.61° and 29.41°, accompanied by pyrene dihedral angles of 44.36° and 41.18°. In contrast, Py-NO_2−COF, bearing electron-withdrawing nitro substituents, exhibits imine dihedral angles of 31.09° and 28.05°, with corresponding pyrene dihedral angles of 43.00° and 46.83°. The introduction of functional groups thus induces moderate torsional distortions, manifesting as a variation of approximately 10° in the imine dihedral angles relative to the unsubstituted Py-

https://doi.org/10.1021/jacs.6c04124
J. Am. Chem. Soc. XXXX, XXX, XXX−XXX

H−COF. These subtle geometric perturbations indicate that, while steric effects do impart a degree of local nonplanarity, they do not severely compromise the overall π-conjugation within the framework.

The HER reaction pathway was further elucidated through Gibbs free energy diagrams (Figure 5g−i). Three potential hydrogen production sites were identified as energetically favorable, including the carbon and nitrogen atoms of the imine units, as well as the carbon atoms of the pyrene units. Among these, the N site in the imine moieties was found to preferentially undergo the proton-coupled reactions. The Gibbs free energy change (ΔG_{H^*}) for the H* intermediate was calculated to be 0.29 eV, −0.18 eV, and −0.02 eV for Py-H−COF (Figure 5g), Py-OMe−COF (Figure 5h), and Py-NO_2−COF (Figure 5i), respectively. This trend can be attributed to the synergistic interaction between the oxygen-containing functional groups in the adjacent phenyl ring and the nitrogen of −C═N− unit, which facilitates proton capture through the formation of an intramolecular six-membered ring hydrogen bond (C═N−H···O). Meanwhile, the existing hydrogen bonds in oxygen-containing structures will restrict the rotation of the linkages, accordingly affecting the flexibility of COFs and further extending the intramolecular π-conjugated. This interaction reduces the ΔG_{H^*}, while enhancing the delocalization of π-electrons, thereby enhancing the efficiency of proton-coupled reactions and the overall photocatalytic HER performance.

CONCLUSIONS

This study advances the development of highly efficient photocatalytic HER systems through the rational design of imine-linked COFs engineered to minimize intralayer polarization while optimizing exciton dissociation and charge-carrier dynamics. A sophisticated molecular engineering strategy was employed to modulate the electronic properties of pyrene-based COFs (Py-R−COFs, where R = −OMe, −H, $-NO_2$) by incorporating functional groups to systematically explore the interplay among imine bond polarization, charge separation, and migration dynamics. This approach is designed to achieve efficient and stable photocatalysis for HER. The integration of electron-donating methoxy (−OMe) groups into the pore walls of Py-OMe-COF effectively attenuates the polarization effect of C═N bonds and reduces interlayer charge repulsion, markedly enhancing the separation and transport of photo-excited charge carriers. Comprehensive photophysical and photoelectrochemical characterizations, including temperature-dependent PL, fs-TAS analysis, and proton conductivity measurements, provide compelling evidence that Py-OMe−COF's distinctive structural and electronic attributes, such as high crystallinity, optimized π−π stacking, prolonged charge carrier lifetimes, and efficient proton transport via the Grötthuss mechanism, synergistically underpin its exceptional photocatalytic HER performance. Conversely, the introduction of electron-withdrawing $-NO_2$ groups in Py-NO_2−COF, despite establishing a D−A configuration, exacerbates polarization, leading to rapid charge recombination and significantly reduced photocatalytic efficiency. These findings establish a rational and effective framework for tuning the polarization characteristics of imine-linked COFs, paving the way for the design of high-performance photocatalysts and advancing sustainable hydrogen production technologies.

ASSOCIATED CONTENT

Supporting Information

The Supporting Information is available free of charge at https://pubs.acs.org/doi/10.1021/jacs.6c04124.

Synthetic details, methods, materials, spectral profiles (e.g., FT-IR, ^{13}C NMR, XPS, etc.), microscopic images (e.g., SEM, TEM, etc.), and computational results (PDF)

AUTHOR INFORMATION

Corresponding Authors

Wei Lin − *State Key Laboratory of Chemistry for NBC Hazards Protection, College of Chemistry, Fuzhou University, Fuzhou 350116, P. R. China; State Key Laboratory of Photocatalysis on Energy and Environment, and Key Laboratory of Advanced Carbon-Based Functional Materials, College of Chemistry, Fuzhou University, Fuzhou 350116, P. R. China;* orcid.org/0000-0002-5046-4765; Email: wlin@fzu.edu.cn

Teng-Teng Chen − *Department of Chemistry, The Hong Kong University of Science and Technology, Kowloon, Hong Kong (SAR) 999077, P. R. China;* orcid.org/0000-0001-9480-615X; Email: tengtengchen@ust.hk

Yihan Zhu − *Center for Electron Microscopy, Zhejiang Key Laboratory of Surface and Interface Science and Engineering for Catalysts, China-Saudi Arabia Joint Laboratory on Microscopic Structural Engineering of Advanced Materials, State Key Laboratory of Green Chemical Synthesis and Conversion and College of Chemical Engineering, Zhejiang University of Technology, Hangzhou 310014, P. R. China;* orcid.org/0000-0002-8150-7350; Email: yihanzhu@zjut.edu.cn

Xiong Chen − *State Key Laboratory of Chemistry for NBC Hazards Protection, College of Chemistry, Fuzhou University, Fuzhou 350116, P. R. China; State Key Laboratory of Photocatalysis on Energy and Environment, and Key Laboratory of Advanced Carbon-Based Functional Materials, College of Chemistry, Fuzhou University, Fuzhou 350116, P. R. China; Sino-UK International Joint Laboratory on Photocatalysis for Clean Energy and Advanced Chemicals & Materials, Fuzhou University, Fuzhou, Fujian 350108, P. R. China;* orcid.org/0000-0003-2878-7522; Email: chenxiong987@fzu.edu.cn

Authors

Zhipeng Luo − *State Key Laboratory of Chemistry for NBC Hazards Protection, College of Chemistry, Fuzhou University, Fuzhou 350116, P. R. China; State Key Laboratory of Photocatalysis on Energy and Environment, and Key Laboratory of Advanced Carbon-Based Functional Materials, College of Chemistry, Fuzhou University, Fuzhou 350116, P. R. China*

Chao Li − *Department of Chemistry, The Hong Kong University of Science and Technology, Kowloon, Hong Kong (SAR) 999077, P. R. China*

Wanxiang Yang − *State Key Laboratory of Chemistry for NBC Hazards Protection, College of Chemistry, Fuzhou University, Fuzhou 350116, P. R. China; State Key Laboratory of Photocatalysis on Energy and Environment, and Key Laboratory of Advanced Carbon-Based Functional*

https://doi.org/10.1021/jacs.6c04124
J. Am. Chem. Soc. XXXX, XXX, XXX−XXX

Materials, College of Chemistry, Fuzhou University, Fuzhou 350116, P. R. China

Yu Chang − *State Key Laboratory of Structural Chemistry, Fujian Provincial Key Laboratory of Materials and Techniques toward Hydrogen Energy, Fujian Institute of Research on the Structure of Matter, Chinese Academy of Sciences, Fuzhou, Fujian 350002, P. R. China*

Kai-Ling Wu − *Department of Chemistry, The Hong Kong University of Science and Technology, Kowloon, Hong Kong (SAR) 999077, P. R. China; Department of Chemistry, State Key Laboratory of Porous Materials for Separation and Conversion, Shanghai Key Laboratory of Molecular Catalysis and Innovative Materials, Fudan University, Shanghai 200438, China*

Liwei Xia − *Center for Electron Microscopy, Zhejiang Key Laboratory of Surface and Interface Science and Engineering for Catalysts, China-Saudi Arabia Joint Laboratory on Microscopic Structural Engineering of Advanced Materials, State Key Laboratory of Green Chemical Synthesis and Conversion and College of Chemical Engineering, Zhejiang University of Technology, Hangzhou 310014, P. R. China*

Jingru Gao − *Center for Electron Microscopy, Zhejiang Key Laboratory of Surface and Interface Science and Engineering for Catalysts, China-Saudi Arabia Joint Laboratory on Microscopic Structural Engineering of Advanced Materials, State Key Laboratory of Green Chemical Synthesis and Conversion and College of Chemical Engineering, Zhejiang University of Technology, Hangzhou 310014, P. R. China*

Fengtao Zhang − *State Key Laboratory of Chemistry for NBC Hazards Protection, College of Chemistry, Fuzhou University, Fuzhou 350116, P. R. China; State Key Laboratory of Photocatalysis on Energy and Environment, and Key Laboratory of Advanced Carbon-Based Functional Materials, College of Chemistry, Fuzhou University, Fuzhou 350116, P. R. China*

Qiwei Duan − *State Key Laboratory of Chemistry for NBC Hazards Protection, College of Chemistry, Fuzhou University, Fuzhou 350116, P. R. China; State Key Laboratory of Photocatalysis on Energy and Environment, and Key Laboratory of Advanced Carbon-Based Functional Materials, College of Chemistry, Fuzhou University, Fuzhou 350116, P. R. China*

Sibo Wang − *State Key Laboratory of Chemistry for NBC Hazards Protection, College of Chemistry, Fuzhou University, Fuzhou 350116, P. R. China; State Key Laboratory of Photocatalysis on Energy and Environment, and Key Laboratory of Advanced Carbon-Based Functional Materials, College of Chemistry, Fuzhou University, Fuzhou 350116, P. R. China;* orcid.org/0000-0003-2656-9169

Zailai Xie − *State Key Laboratory of Chemistry for NBC Hazards Protection, College of Chemistry, Fuzhou University, Fuzhou 350116, P. R. China; State Key Laboratory of Photocatalysis on Energy and Environment, and Key Laboratory of Advanced Carbon-Based Functional Materials, College of Chemistry, Fuzhou University, Fuzhou 350116, P. R. China;* orcid.org/0000-0002-7694-7634

Xiaofeng Wu − *Materials Innovation Factory, Department of Chemistry, University of Liverpool, Liverpool L69 7ZD, U.K.; Sino-UK International Joint Laboratory on Photocatalysis for Clean Energy and Advanced Chemicals & Materials, Fuzhou University, Fuzhou, Fujian 350108, P. R. China*

Guan-E Wang − *State Key Laboratory of Structural Chemistry, Fujian Provincial Key Laboratory of Materials and Techniques toward Hydrogen Energy, Fujian Institute of Research on the Structure of Matter, Chinese Academy of Sciences, Fuzhou, Fujian 350002, P. R. China;* orcid.org/0000-0001-9523-0631

Mingfei Zhou − *Department of Chemistry, State Key Laboratory of Porous Materials for Separation and Conversion, Shanghai Key Laboratory of Molecular Catalysis and Innovative Materials, Fudan University, Shanghai 200438, China;* orcid.org/0000-0002-1915-6203

Gang Xu − *State Key Laboratory of Structural Chemistry, Fujian Provincial Key Laboratory of Materials and Techniques toward Hydrogen Energy, Fujian Institute of Research on the Structure of Matter, Chinese Academy of Sciences, Fuzhou, Fujian 350002, P. R. China;* orcid.org/0000-0001-8562-0724

Complete contact information is available at: https://pubs.acs.org/10.1021/jacs.6c04124

Author Contributions

○Z.L., C.L., W.Y. and Y.C. contributed equally to this work.

Notes

The authors declare no competing financial interest.

■ ACKNOWLEDGMENTS

This work was financially supported by the National Key Research and Development Program of China (2021YFA1502100, 2022YFE0113800), the National Natural Science Foundation of China (22572031, 22122505, 22075250, 21771161), the Natural Science Foundation of Fujian Province (2024J01238), the Zhejiang Provincial Natural Science Foundation of China (LBMHz25B030005). Teng-Teng Chen acknowledges the start-up fund (R9874) from HKUST, Early Career Scheme (26311224) and General Research Fund (16312125) from the Research Grants Council of Hong Kong, Science and Technology Cooperation Project with Hong Kong, Macao and Taiwan of Yancheng (Ycgh2025008), Guangdong Basic and Applied Basic Research Foundation (2026A1515010657), and open research fund of State Key Laboratory of Optical Quantum Materials at the University of Hong Kong.

■ REFERENCES

(1) (a) Nishioka, S.; Osterloh, F. E.; Wang, X.; Mallouk, T. E.; Maeda, K. Photocatalytic water splitting. *Nat. Rev. Methods Primers* **2023**, *3*, 42. (b) Wang, Z.; Hisatomi, T.; Li, R.; Sayama, K.; Liu, G.; Domen, K.; Li, C.; Wang, L. Efficiency Accreditation and Testing Protocols for Particulate Photocatalysts toward Solar Fuel Production. *Joule* **2021**, *5*, 344−359.

(2) (a) Tan, D.; Zhuang, R.; Chen, R.; Ban, M.; Feng, W.; Xu, F.; Chen, X.; Wang, Q. Covalent Organic Frameworks Enable Sustainable Solar to Hydrogen Peroxide. *Adv. Funct. Mater.* **2023**, *34*, 2311655. (b) Jiang, D.; Tan, V. G. W.; Gong, Y.; Shao, H.; Mu, X.; Luo, Z.; He, S. Semiconducting Covalent Organic Frameworks. *Chem. Rev.* **2025**, *125*, 6203−6308. (c) Zeng, X.; Guo, M.; Wang, L.; Xu, H.; Lin, C.; Luo, Z.; Zhang, F.; Zhu, S.; Wang, S.; Fang, Y.; Lin, W.; Chen, X. Conformational Control of Ni Coordination Sites in Pyridyl-Functionalized Covalent Organic Frameworks for Exceptional CO2 photoreduction. *Sci. Bull.* **2025**, *70*, 2725−2729. (d) Lu, J.; Lin, C.; Li, C.; Shi, H.; Liu, N.; Xing, W.; Wang, S.; Zhang, G.; Chen, T.-T.; Chen, X. Bipyridine-integrated bisoxazole-based donor-acceptor covalent organic framework for enhanced photocatalytic H_2O_2 synthesis. *Chin. J. Catal.* **2026**, *81*, 185−194. (e) Xu, H.; Xia, S.; Li, C.; Li, Y.; Xing, W.; Jiang, Y.; Chen, X. Programming

Tetrathiafulvalene-Based Covalent Organic Frameworks for Promoted Photoinduced Molecular Oxygen Activation. *Angew. Chem.* **2024**, *136*, No. e202405476. (f) Ma, S.; Li, Z.; Jia, J.; Zhang, Z.; Xia, H.; Li, H.; Chen, X.; Xu, Y.; Liu, X. Amide-linked covalent organic frameworks as efficient heterogeneous photocatalysts in water. *Chin. J. Catal.* **2021**, *42*, 2010−2019.

(3) (a) Manzoor, S.; Younis, M. A.; Yao, Y.; Tariq, Q.-u.-n.; Zhang, B.; Tian, B.; Yan, L.; Qiu, C. Schiff base COFs for photocatalysis: From fundamentals to applications. *Coord. Chem. Rev.* **2025**, *541*, 216840. (b) Li, Z.; Liu, C.; Deng, Q.; Deng, W. Rational Design of Covalent Organic Frameworks as Photocatalysts for Water Splitting. *Adv. Funct. Mater.* **2024**, *34*, 2402676. (c) Zhu, S.; Luo, Z.; Zhang, F.; Huang, Y.; Yang, W.; Xiong, Y.; Zhang, R.; Yu, Z.; Lin, C.; Zeng, X.; Xu, S.; Li, Y.; Lin, W.; Chen, J.; Chen, X. Fluorination-Modulated Molecular Engineering in β-Ketoenamine Covalent Organic Frameworks toward Efficient Photocatalytic Hydrogen Evolution. *Chin. J. Chem.* **2025**, *43*, 3397−3404. (d) Zhou, P. K.; Liang, C.; Zhang, C.; Huang, Y.; Yu, Z.; Lin, C.; Zhang, C.; Sun, Q.; Song, Y.; Ren, X.-R.; Wang, D.; Wang, S.; Lam, Y. M.; Chen, X. Tuning Protonation Microenvironments via Edge-Linker Design in One-Dimensional Imine-Linked Covalent Organic Frameworks for Efficient Photocatalytic Hydrogen Evolution. *ACS Catal.* **2025**, *15*, 16992−17002. (e) Liu, H.; Wang, D.; Yu, Z.; Chen, Y.; Li, X.; Zhang, R.; Chen, X.; Wu, L.; Ding, N.; Wang, Y.; Zhao, Y. Fully conjugated two-dimensional sp^2-carbon covalent organic frameworks for efficient photocatalytic hydrogen generation. *Sci. China Mater.* **2023**, *66*, 2283−2289. (f) Xie, Z.; Yang, X.; Zhang, P.; Ke, X.; Yuan, X.; Zhai, L.; Wang, W.; Qin, N.; Cui, C.-X.; Qu, L.; Chen, X. Vinylene-linked covalent organic frameworks with manipulated electronic structure for efficient solar-driven photocatalytic hydrogen production. *Chin. J. Catal.* **2023**, *47*, 171−180.

(4) (a) Nath, I.; Chakraborty, J.; Rawat, K. S.; Ji, Y.; Wang, R.; Molkens, K.; De Geyter, N.; Morent, R.; Van Speybroeck, V.; Geiregat, P.; Van Der Voort, P. Mesoporous Acridinium-Based Covalent Organic Framework for Long-lived Charge-Separated Exciton Mediated Photocatalytic [4 + 2] Annulation. *Adv. Mater.* **2025**, *37*, 2413060. (b) Wang, H.; Jin, S.; Zhang, X.; Xie, Y. Excitonic Effects in Polymeric Photocatalysts. *Angew. Chem., Int. Ed.* **2020**, *59*, 22828−22839. (c) Lan, Z. A.; Wu, M.; Fang, Z.; Chi, X.; Chen, X.; Zhang, Y.; Wang, X. A Fully Coplanar Donor-Acceptor Polymeric Semiconductor with Promoted Charge Separation Kinetics for Photochemistry. *Angew. Chem., Int. Ed.* **2021**, *60*, 16355−16359. (d) Lan, Z. A.; Zhang, G.; Chen, X.; Zhang, Y.; Zhang, K. A. I.; Wang, X. Reducing the Exciton Binding Energy of Donor-Acceptor-Based Conjugated Polymers to Promote Charge-Induced Reactions. *Angew. Chem., Int. Ed.* **2019**, *58*, 10236−10240.

(5) (a) Rodriguez-Camargo, A.; Endo, K.; Lotsch, B. V. Celebrating Ten Years of Covalent Organic Frameworks for Solar Energy Conversion: Past, Present and Future. *Angew. Chem., Int. Ed.* **2024**, *63*, No. e202413096. (b) Mishra, B.; Alam, A.; Chakraborty, A.; Kumbhakar, B.; Ghosh, S.; Pachfule, P.; Thomas, A. Covalent Organic Frameworks for Photocatalysis. *Adv. Mater.* **2025**, *37*, 2413118. (c) Zhao, Z.; Chen, X.; Li, B.; Zhao, S.; Niu, L.; Zhang, Z.; Chen, Y. Spatial Regulation of Acceptor Units in Olefin-Linked COFs toward Highly Efficient Photocatalytic H_2 Evolution. *Adv. Sci.* **2022**, *9*, 2203832.

(6) (a) Qian, C.; Feng, L.; Teo, W. L.; Liu, J.; Zhou, W.; Wang, D.; Zhao, Y. Imine and imine-derived linkages in two-dimensional covalent organic frameworks. *Nat. Rev. Chem.* **2022**, *6*, 881−898. (b) Tan, K. T.; Ghosh, S.; Wang, Z.; Wen, F.; Rodríguez-San-Miguel, D.; Feng, J.; Huang, N.; Wang, W.; Zamora, F.; Feng, X.; Thomas, A.; Jiang, D. Covalent organic frameworks. *Nat. Rev. Methods Primers* **2023**, *3*, 1. (c) Yu, H.; Zhang, F.; Chen, Q.; Zhou, P. K.; Xing, W.; Wang, S.; Zhang, G.; Jiang, Y.; Chen, X. Vinyl-Group-Anchored Covalent Organic Framework for Promoting the Photocatalytic Generation of Hydrogen Peroxide. *Angew. Chem., Int. Ed.* **2024**, *63*, No. e202402297.

(7) (a) Chen, X.; Addicoat, M.; Irle, S.; Nagai, A.; Jiang, D. Control of crystallinity and porosity of covalent organic frameworks by managing interlayer interactions based on self-complementary π-electronic force. *J. Am. Chem. Soc.* **2013**, *135*, 546−549. (b) Uribe-Romo, F. J.; Hunt, J. R.; Furukawa, H.; Klock, C.; O'Keeffe, M.; Yaghi, O. M. A crystalline imine-linked 3-D porous covalent organic framework. *J. Am. Chem. Soc.* **2009**, *131*, 4570−4571. (c) Chen, X.; Addicoat, M.; Jin, E.; Zhai, L.; Xu, H.; Huang, N.; Guo, Z.; Liu, L.; Irle, S.; Jiang, D. Locking covalent organic frameworks with hydrogen bonds: general and remarkable effects on crystalline structure, physical properties, and photochemical activity. *J. Am. Chem. Soc.* **2015**, *137*, 3241−3247. (d) Chen, X.; Huang, N.; Gao, J.; Xu, H.; Xu, F.; Jiang, D. Towards covalent organic frameworks with predesignable and aligned open docking sites. *Chem. Commun.* **2014**, *50*, 6161−6163. (e) Wu, Y.; Xu, H.; Chen, X.; Gao, J.; Jiang, D. A π-electronic covalent organic framework catalyst: π-walls as catalytic beds for Diels-Alder reactions under ambient conditions. *Chem. Commun.* **2015**, *51*, 10096−10098. (f) Vitaku, E.; Dichtel, W. R. Synthesis of 2D Imine-Linked Covalent Organic Frameworks through Formal Transimination Reactions. *J. Am. Chem. Soc.* **2017**, *139*, 12911−12914.

(8) (a) Waller, P. J.; AlFaraj, Y. S.; Diercks, C. S.; Jarenwattananon, N. N.; Yaghi, O. M. Conversion of Imine to Oxazole and Thiazole Linkages in Covalent Organic Frameworks. *J. Am. Chem. Soc.* **2018**, *140*, 9099−9103. (b) Cusin, L.; Peng, H.; Ciesielski, A.; Samori, P. Chemical Conversion and Locking of the Imine Linkage: Enhancing the Functionality of Covalent Organic Frameworks. *Angew. Chem., Int. Ed.* **2021**, *60*, 14236−14250. (c) Yan, X.; Wang, F.; Su, X.; Ren, J.; Qi, M.; Bao, P.; Chen, W.; Peng, C.; Chen, L. A Redox-Active Covalent Organic Framework with Highly Accessible Aniline-Fused Quinonoid Units Affords Efficient Proton Charge Storage. *Adv. Mater.* **2023**, *35*, 2305037. (d) Xie, Z.; Chen, X.; Wang, W.; Ke, X.; Zhang, X.; Wang, S.; Wu, X.; Yu, J. C.; Wang, X. Variation of Chemical Microenvironment of Pores in Hydrazone-Linked Covalent Organic Frameworks for Photosynthesis of H_2O_2. *Angew. Chem., Int. Ed.* **2024**, *63*, No. e202410179. (e) Hao, Q.; Tao, Y.; Ding, X.; Yang, Y.; Feng, J.; Wang, R.-L.; Chen, X.-M.; Chen, G.-L.; Li, X.; OuYang, H.; Hu, X. L.; Tian, J.; Han, B.-H.; Zhu, G.; Wang, W.; Zhang, F.; Tan, B.; Li, Z.-T.; Wang, D.; Wan, L.-J. Porous organic polymers: a progress report in China. *Sci. China Chem.* **2023**, *66*, 620−682. (f) Chai, S.; Chen, X.; Zhang, X.; Fang, Y.; Sprick, R. S.; Chen, X. Rational Design of Covalent Organic Frameworks for Efficient Photocatalytic Hydrogen Peroxide Production. *Environ. Sci.:Nano* **2022**, *9*, 2464−2469.

(9) (a) Yang, J.; Acharjya, A.; Ye, M. Y.; Rabeah, J.; Li, S.; Kochovski, Z.; Youk, S.; Roeser, J.; Gruneberg, J.; Penschke, C.; Schwarze, M.; Wang, T.; Lu, Y.; van de Krol, R.; Oschatz, M.; Schomacker, R.; Saalfrank, P.; Thomas, A. Protonated Imine-Linked Covalent Organic Frameworks for Photocatalytic Hydrogen Evolution. *Angew. Chem., Int. Ed.* **2021**, *60*, 19797−19803. (b) Yang, J.; Ghosh, S.; Roeser, J.; Acharjya, A.; Penschke, C.; Tsutsui, Y.; Rabeah, J.; Wang, T.; Djoko Tameu, S. Y.; Ye, M. Y.; Gruneberg, J.; Li, S.; Li, C.; Schomacker, R.; Van De Krol, R.; Seki, S.; Saalfrank, P.; Thomas, A. Constitutional isomerism of the linkages in donor-acceptor covalent organic frameworks and its impact on photocatalysis. *Nat. Commun.* **2022**, *13*, 6317. (c) Dong, W.; Qin, Z.; Wang, K.; Xiao, Y.; Liu, X.; Ren, S.; Li, L. Isomeric Oligo(Phenylenevinylene)-Based Covalent Organic Frameworks with Different Orientation of Imine Bonds and Distinct Photocatalytic Activities. *Angew. Chem., Int. Ed.* **2023**, *62*, No. e202216073. (d) Liu, N.; Xie, S.; Huang, Y.; Lu, J.; Shi, H.; Xu, S.; Zhang, G.; Chen, X. Dual-Acceptor Engineering in Pyrene-Based Covalent Organic Frameworks for Boosting Photocatalytic Hydrogen Evolution. *Adv. Energy Mater.* **2024**, *14*, 2402395.

(10) (a) Zou, L.; Si, D.; Yang, S.; Chen, Z.; Huang, Y.; Cao, R. Induced Charge-Compensation Effect for Boosting Photocatalytic Water Splitting in Covalent Organic Frameworks. *Angew. Chem., Int. Ed.* **2025**, *64*, No. e202418319. (b) Xu, H.; Gao, J.; Jiang, D. Stable, crystalline, porous, covalent organic frameworks as a platform for chiral organocatalysts. *Nat. Chem.* **2015**, *7*, 905−912.

(11) (a) Li, Z.; Cai, B.; Li, Q.; Zhang, D.; Liang, Y.; Liu, Y.; Jiao, Y.; Thomas, A.; Zhao, X. Modulating the Polarity of Imine Bonds in Donor-Acceptor Covalent Organic Frameworks for Enhanced Photo-

https://doi.org/10.1021/jacs.6c04124
J. Am. Chem. Soc. XXXX, XXX, XXX−XXX

catalytic H_2 Production. *Angew. Chem., Int. Ed.* **2025**, *64*, No. e202509444. (b) Yang, S.; Si, D.; Zou, L.; Shi, M.; Huang, Y.; Cao, R. Engineering Imine Carbon Catalytic Sites in Covalent Organic Frameworks for Enhanced Overall H_2O_2 Photosynthesis. *J. Am. Chem. Soc.* **2025**, *147*, 30287−30295.

(12) (a) Yang, S.; Yang, C.; Dun, C.; Mao, H.; Khoo, R. S. H.; Klivansky, L. M.; Reimer, J. A.; Urban, J. J.; Zhang, J.; Liu, Y. Covalent Organic Frameworks with Irreversible Linkages via Reductive Cyclization of Imines. *J. Am. Chem. Soc.* **2022**, *144*, 9827−9835. (b) Li, X. T.; Zou, J.; Wang, T. H.; Ma, H. C.; Chen, G. J.; Dong, Y. B. Construction of Covalent Organic Frameworks via Three-Component One-Pot Strecker and Povarov Reactions. *J. Am. Chem. Soc.* **2020**, *142*, 6521−6526.

(13) (a) Deng, X.; Gao, N.; Bai, L. Bromine Atoms Decorated Pyene-based Covalent Organic Frameworks for Accelerated Photocatalytic H_2 Production. *Small* **2024**, *20*, 2311927. (b) Yang, Y.; Kang, J.; Li, Y.; Liang, J.; Liang, J.; Jiang, L.; Chen, D.; He, J.; Chen, Y.; Wang, J. Enhanced photocatalytic hydrogen peroxide production activity of imine-linked covalent organic frameworks via modification with functional groups. *New J. Chem.* **2022**, *46*, 21605−21614. (c) Zhang, Y.; Cao, Q.; Meng, A.; Wu, X.; Xiao, Y.; Su, C.; Zhang, Q. Molecular Heptazine-Triazine Junction over Carbon Nitride Frameworks for Artificial Photosynthesis of Hydrogen Peroxide. *Adv. Mater.* **2023**, *35*, 2306831.

(14) (a) Zhu, Y.; Ciston, J.; Zheng, B.; Miao, X.; Czarnik, C.; Pan, Y.; Sougrat, R.; Lai, Z.; Hsiung, C. E.; Yao, K.; Pinnau, I.; Pan, M.; Han, Y. Unravelling surface and interfacial structures of a metal-organic framework by transmission electron microscopy. *Nat. Mater.* **2017**, *16*, 532−536. (b) Chen, Q.; Dwyer, C.; Sheng, G.; Zhu, C.; Li, X.; Zheng, C.; Zhu, Y. Imaging Beam-Sensitive Materials by Electron Microscopy. *Adv. Mater.* **2020**, *32*, 1907619. (c) Liu, Y.; Liu, X.; Su, A.; Gong, C.; Chen, S.; Xia, L.; Zhang, C.; Tao, X.; Li, Y.; Li, Y.; Sun, T.; Bu, M.; Shao, W.; Zhao, J.; Li, X.; Peng, Y.; Guo, P.; Han, Y.; Zhu, Y. Revolutionizing the structural design and determination of covalent-organic frameworks: principles, methods, and techniques. *Chem. Soc. Rev.* **2024**, *53*, 502−544. (d) Wang, S.; Liang, K.; Zhao, H.; Wu, M.; He, J.; Wei, P.; Ding, Z.; Li, J.; Huang, X.; Ren, Y. Electronic structure formed by Y_2O_3-doping in lithium position assists improvement of charging-voltage for high-nickel cathodes. *Nat. Commun.* **2025**, *16*, 1. (e) Zhang, W.; Jiang, H.; Liu, Y.; Hu, Y.; Palakkal, A. S.; Zhou, Y.; Sun, M.; Du, E.; Gong, W.; Zhang, Q.; Jiang, J.; Dong, J.; Liu, Y.; Li, D.; Zhu, Y.; Cui, Y.; Duan, X. Metal-halide porous framework superlattices. *Nature* **2025**, *638*, 418−424.

(15) (a) Luo, Z.; Zhu, S.; Xue, H.; Yang, W.; Zhang, F.; Xu, F.; Lin, W.; Wang, H.; Chen, X. Manipulating p-π Resonance through Methoxy Group Engineering in Covalent Organic Frameworks for an Efficient Photocatalytic Hydrogen Evolution. *Angew. Chem.* **2025**, *64*, No. e202420217. (b) Luo, Z.; Chen, X.; Hu, Y.; Chen, X.; Lin, W.; Wu, X.; Wang, X. Side-Chain Molecular Engineering of Triazole-Based Donor-Acceptor Polymeric Photocatalysts with Strong Electron Push-Pull Interactions. *Angew. Chem.* **2023**, *62*, No. e202304875. (c) Liu, F.; He, Y.; Liu, X.; Wang, Z.; Liu, H.-L.; Zhu, X.; Hou, C.-C.; Weng, Y.; Zhang, Q.; Chen, Y. Regulating Excitonic Effects in Covalent Organic Frameworks to Promote Free Charge Carrier Generation. *ACS Catal.* **2022**, *12*, 9494−9502. (d) Wang, L.; Xie, Z.; Zeng, X.; Xu, H.; Wang, M.; Yang, J.; Lin, C.; Xing, W.; Guo, Z.; Chen, X. Fused Ring Engineering Induced Topology Control in Covalent Organic Frameworks: Unlocking Promoted Photocatalytic H_2O_2 Production and Selective Methane Oxidation. *Angew. Chem.* **2026**, No. e1288153. (e) Xie, Z.; Wang, W.; Ke, X.; Cai, X.; Chen, X.; Wang, S.; Lin, W.; Wang, X. A Heptazine-Based Polymer Photocatalyst with Donor-Acceptor Configuration to Promote Exciton Dissociation and Charge Separation. *Appl. Catal., B* **2023**, *325*, 122312.

(16) (a) Fu, Z.; Wang, X.; Gardner, A. M.; Wang, X.; Chong, S. Y.; Neri, G.; Cowan, A. J.; Liu, L.; Li, X.; Vogel, A.; Clowes, R.; Bilton, M.; Chen, L.; Sprick, R. S.; Cooper, A. I. A stable covalent organic framework for photocatalytic carbon dioxide reduction. *Chem. Sci.* **2020**, *11*, 543−550. (b) Feng, T.; Streater, D.; Sun, B.; Duisenova, K.; Wang, D.; Liu, Y.; Huang, J.; Zhang, J. Tuning Photoexcited Charge Transfer in Imine-Linked Two-Dimensional Covalent Organic Frameworks. *J. Phys. Chem. Lett.* **2022**, *13*, 1398−1405. (c) Li, C.; Liu, J.; Li, H.; Wu, K.; Wang, J.; Yang, Q. Covalent organic frameworks with high quantum efficiency in sacrificial photocatalytic hydrogen evolution. *Nat. Commun.* **2022**, *13*, 2357.

(17) Lin, Z.; Yu, X.; Zhao, Z.; Ding, N.; Wang, C.; Hu, K.; Zhu, Y.; Guo, J. Controlling crystallization in covalent organic frameworks to facilitate photocatalytic hydrogen production. *Nat. Commun.* **2025**, *16*, 1940.

(18) (a) Wang, Q.; Zhang, G.; Xing, W.; Pan, Z.; Zheng, D.; Wang, S.; Hou, Y.; Wang, X. Bottom-up Synthesis of Single-Crystalline Poly (Triazine Imide) Nanosheets for Photocatalytic Overall Water Splitting. *Angew. Chem., Int. Ed.* **2023**, *135*, No. e202307930. (b) Ruan, X.; Cui, X.; Cui, Y.; Fan, X.; Li, Z.; Xie, T.; Ba, K.; Jia, G.; Zhang, H.; Zhang, L.; Zhang, W.; Zhao, X.; Leng, J.; Jin, S.; Singh, D. J.; Zheng, W. Favorable Energy Band Alignment of TiO_2 Anatase/Rutile Heterophase Homojunctions Yields Photocatalytic Hydrogen Evolution with Quantum Efficiency Exceeding 45.6%. *Adv. Energy Mater.* **2022**, *12*, 2200298. (c) Li, S.; Hou, L. B.; Zhang, L. J.; Chen, L. P.; Lin, Y. H.; Wang, D. J.; Xie, T. F. Direct evidence of the efficient hole collection process of the CoOx cocatalyst for photocatalytic reactions: a surface photovoltage study. *J. Mater. Chem. A* **2015**, *3*, 17820−17826.

(19) Luo, Z.; Chen, X.; Yang, W.; Chang, Y.; Zhu, S.; Zhang, F.; Lin, W.; Xu, G.; Wang, G.-E.; Chen, X. Modulating pyrene-based covalent organic framework via BF_2 functionalization for facilitated photocatalytic proton-coupled electron-transfer reductions. *Sci. China Chem.* **2025**, *68*, 6639−6647.

(20) (a) Chen, J.; An, B.; Chen, Y.; Han, X.; Mei, Q.; He, M.; Cheng, Y.; Vitorica-Yrezabal, I. J.; Natrajan, L. S.; Lee, D.; Ramirez-Cuesta, A. J.; Yang, S.; Schroder, M. Ultra-fast Proton Conduction and Photocatalytic Water Splitting in a Pillared Metal-Organic Framework. *J. Am. Chem. Soc.* **2023**, *145*, 19225−19231. (b) Guan, L.; Guo, Z.; Zhou, Q.; Zhang, J.; Cheng, C.; Wang, S.; Zhu, X.; Dai, S.; Jin, S. A highly proton conductive perfluorinated covalent triazine framework via low-temperature synthesis. *Nat. Commun.* **2023**, *14*, 8114. (c) Lin, Y.; Zou, J.; Wu, X.; Tong, S.; Niu, Q.; He, S.; Luo, S.; Yang, C. Efficient Proton Transfer and Charge Separation within Covalent Organic Frameworks via Hydrogen-Bonding Network to Boost H_2O_2 Photosynthesis. *Nano Lett.* **2024**, *24*, 6302−6311.

(21) Yang, J.; Xu, H.; Li, J.; Gong, K.; Yue, F.; Han, X.; Wu, K.; Shao, P.; Fu, Q.; Zhu, Y.; Xu, W.; Huang, X.; Xie, J.; Wang, F.; Yang, W.; Zhang, T.; Xu, Z.; Feng, X.; Wang, B. Oxygen- and proton-transporting open framework ionomer for medium-temperature fuel cells. *Science* **2024**, *385*, 1115−1120.

(22) (a) Shi, B.; Pang, X.; Li, S.; Wu, H.; Shen, J.; Wang, X.; Fan, C.; Cao, L.; Zhu, T.; Qiu, M.; Yin, Z.; Kong, Y.; Liu, Y.; Zhang, M.; Liu, Y.; Pan, F.; Jiang, Z. Short hydrogen-bond network confined on COF surfaces enables ultrahigh proton conductivity. *Nat. Commun.* **2022**, *13*, 6666. (b) Guo, R.; Zhou, Y.; Wang, W.; Zhai, Y.; Liu, X.; He, W.; Ou, W.; Ding, R.; Zhang, H. L.; Wu, M.; Jiang, Z.; Zhou, K. G. Interlayer confinement toward short hydrogen bond network construction for fast hydroxide transport. *Sci. Adv.* **2025**, *11*, No. eadr5374. (c) Qiu, L.; Tian, F.; He, L.; Li, M.; Lin, F.; Li, L.; Ren, X.; Wu, F.; Li, L.; Zhang, T.; Sheng, J.; Yu, Y.; Yang, W.; Guo, S. Robust Interfacial Hydrogen-Bond Network on Positively Charged Ru-N-Ni Dual Sites Boosts Alkaline Hydrogen Electrocatalysis. *Adv. Mater.* **2026**, *38*, No. e12568. (d) Iwano, T.; Akutsu, D.; Ubukata, H.; Ogiwara, N.; Kikukawa, Y.; Wang, S.; Yan, L. K.; Kageyama, H.; Uchida, S. Tuning Proton Conduction by Staggered Arrays of Polar Preyssler-Type Oxoclusters. *J. Am. Chem. Soc.* **2024**, *146*, 26113−26120.

(23) (a) Lu, X.; Zhang, Y.; Ma, X.; Yuan, C.; Chen, Y.; Guo, J.; Gao, D.; Tu, Y.; Liu, Q.; Wang, J.; Wei, Z. Hydrogen Bond Network Assisted Ultrafast Ion Transport of Anion Exchange Membrane Grafting with Covalent Organic Frameworks for Hydrogen Conversion. *Angew. Chem.* **2025**, *64*, No. e202503372. (b) Zheng, X.; Cui, Y. M.; Wang, N. H.; Wu, X. S.; Su, Z. M.; Han, X. Q.

https://doi.org/10.1021/jacs.6c04124
J. Am. Chem. Soc. XXXX, XXX, XXX−XXX

Uncoordinated Carboxyl Groups as Proton Sources in Polyoxometalate-Based Metal-Organic Frameworks Enhance Proton Conduction. *Inorg. Chem.* **2024**, *63*, 24232−24239.

https://doi.org/10.1021/jacs.6c04124
J. Am. Chem. Soc. XXXX, XXX, XXX−XXX